

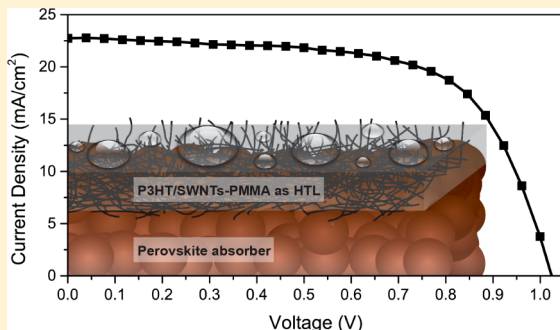
Carbon Nanotube/Polymer Composites as a Highly Stable Hole Collection Layer in Perovskite Solar Cells

Severin N. Habisreutinger, Tomas Leijtens, Giles E. Eperon, Samuel D. Stranks, Robin J. Nicholas, and Henry J. Snaith*

Department of Physics, University of Oxford, Clarendon Laboratory, Parks Road, Oxford OX1 3PU, United Kingdom

S Supporting Information

ABSTRACT: Organic–inorganic perovskite solar cells have recently emerged at the forefront of photovoltaics research. Power conversion efficiencies have experienced an unprecedented increase to reported values exceeding 19% within just four years. With the focus mainly on efficiency, the aspect of stability has so far not been thoroughly addressed. In this paper, we identify thermal stability as a fundamental weak point of perovskite solar cells, and demonstrate an elegant approach to mitigating thermal degradation by replacing the organic hole transport material with polymer-functionalized single-walled carbon nanotubes (SWNTs) embedded in an insulating polymer matrix. With this composite structure, we achieve JV scanned power-conversion efficiencies of up to 15.3% with an average efficiency of $10 \pm 2\%$. Moreover, we observe strong retardation in thermal degradation as compared to cells employing state-of-the-art organic hole-transporting materials. In addition, the resistance to water ingress is remarkably enhanced. These are critical developments for achieving long-term stability of high-efficiency perovskite solar cells.



KEYWORDS: Photovoltaics, perovskite solar cells, single-walled carbon nanotubes, polymer functionalization, hole-transport materials, stability

The conversion of solar energy into electricity is one of the most promising routes to meeting the increasing energy demands of future generations without negatively impacting the global climate.¹ The cost and energy input involved in the manufacturing process are crucial challenges faced by the existing solar cell industry, both of which can be reduced by newly emerging thin-film and organic–inorganic hybrid concepts.² However, since a large fraction of the cost of photovoltaic solar energy is incurred by elements beyond the actual solar cells and modules, such as inverters, frames, land and installation, in order for any emerging photovoltaic technology to become competitive, both high efficiency as well as long-term stability are required. Important breakthroughs in device performance have recently been achieved through the use of semiconducting organic–inorganic perovskite absorbers.^{3–8} Remarkably, the organic–inorganic lead halide perovskites can function both as a broad-band absorber and as an ambipolar charge transporter.^{3,9,10} The latter property allows it to be coated onto an electronically inert alumina scaffold forming the basis for the architecture ‘meso-superstructured solar cells’ (MSSCs), or to be employed in a planar heterojunction device. In both architectures charge generation and transport occur within the perovskite material yielding scanned power-conversion efficiencies of more than 15% and 19%, respectively.^{6,11–13}

Following light absorption, charge is generated within the bulk of the perovskite absorber, but efficient charge extraction

requires selective contacting of the perovskite layer with a positive (p) and a negative (n) contact material, which should both exhibit low resistive losses.¹⁶ Efficient extraction of the p-type charges (holes) is usually achieved with a hole-selective transport layer which prevents charge recombination at the metallic cathode. High-performance perovskite solar cells generally employ a p-type organic small-molecule or polymeric hole-conductor, such as 2,2',7,7'-tetrakis(*N,N*-di-*p*-methoxyphenylamine)-9,9'-spirobifluorene (spiro-OMeTAD), poly(3-hexylthiophene) (P3HT), or poly(triarylamine) (PTAA) to achieve the highest efficiencies.^{6,8,11,12,17–19} The intrinsically low hole mobility of the amorphous spiro-OMeTAD can be overcome to a certain extent by increasing the carrier density by oxidative doping.^{20–23} Lithium salts are most commonly used as effective p-dopants in the presence of oxygen.²⁴ Despite higher intrinsic hole mobilities compared to their amorphous counterpart, polymeric hole-conductors generally still need to be p-doped in order to achieve comparably high photocurrents.^{17,25}

Having demonstrated that high efficiencies can be attained, with foreseeable routes to even further improvements, one of the biggest remaining challenges for perovskite solar cells, with regards to their commercial viability, is the aspect of long-term

Received: May 27, 2014

Revised: September 8, 2014

Published: September 16, 2014



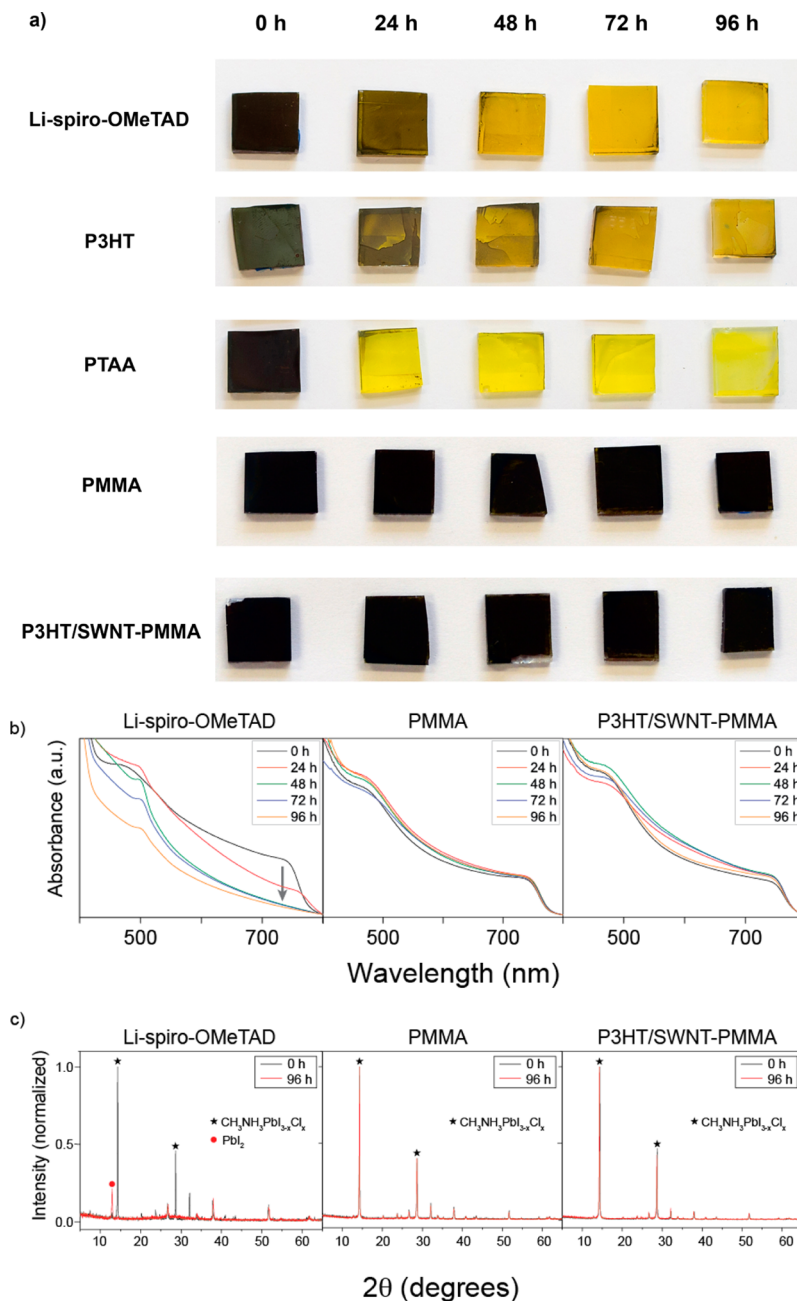


Figure 1. Illustration of the protective effect of various materials on top of perovskite films under thermal stressing. (a) Photo illustrating the visible degradation of the perovskite layer. The color shifts from almost black to yellow for all organic HTLs except for the films covered with PMMA only or a composite of carbon nanotubes and PMMA. (b) Changes in the absorption spectra taken at 24 h intervals. The sample with Li-spiro-OMeTAD, being representative of the degrading organic HTLs, loses the perovskite characteristic absorption onset (indicated by the gray arrow). (c) X-ray diffraction pattern of devices before (black line) and after (red line) 96 h heat exposure. The spectral changes from the diffraction features characteristic for the $\text{CH}_3\text{NH}_3\text{PbI}_{3-x}\text{Cl}_x$ at 14.28° and 28.57° (black star) to a new diffraction feature at 12.80° associated with PbI_2 indicate degradation of the perovskite crystal structure. For the neat PMMA layer and the PMMA-nanotube composite HTL, there are no discernible changes in the diffraction patterns.

stability, in particular when subjected to environmental stresses such as moisture and heating cycles. One weakness of the methylammonium lead halide perovskites is their inherent vulnerability to moisture and heat, but little work has been done with respect to examining how working perovskite solar cells react to these external variables. Reported stability measurements have thus far been limited to temperature regimes below 50°C ,^{8,26–28} which is why there is a clear need for further studies on the stability of perovskite solar cells in higher temperature regimes. Here, we show that the conven-

tional state-of-the-art perovskite solar cells employing organic hole-transporters are extremely sensitive to elevated temperature and moisture. We replace the organic hole-transporters with a conducting carbon-nanotube-insulating polymer composite, which yields efficient solar cells with greatly enhanced stability to thermal stressing and water exposure.

We subjected a bare layer of fully crystallized $\text{CH}_3\text{NH}_3\text{PbI}_{3-x}\text{Cl}_x$ perovskite film to a temperature of 80°C in air, which lead to a fast degradation of its structure characterized by a color change from dark brown to yellow

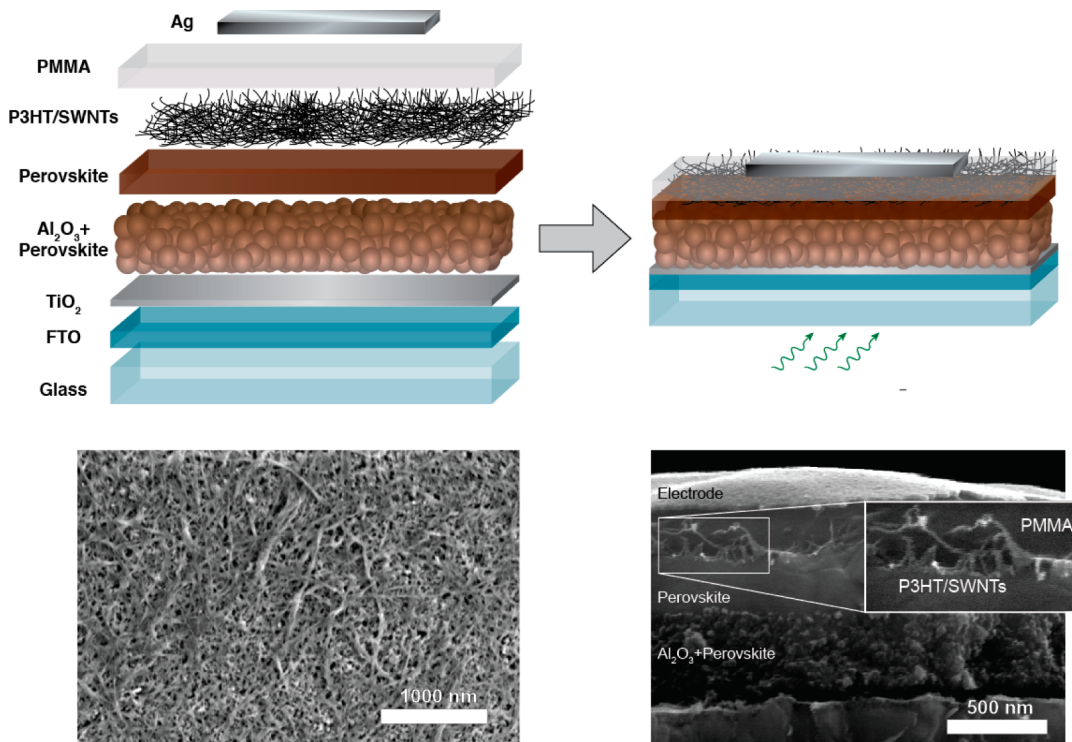


Figure 2. Schematic illustration of the solar cell with a carbon nanotube/polymer composite as hole-transporting structure. Schematic architecture of the investigated device consisting of sequential layers of FTO as transparent electrode, a TiO₂ compact layer, a mesostructured layer of Al₂O₃ coated with CH₃NH₃PbI_{3-x}Cl_x and the hole transporting structure composed of a P3HT/SWNT layer in-filled with a PMMA matrix.

(Supporting Information 1). This color change is thought to be associated with a transformation of the perovskite crystal structure to a zero-dimensional system in which the individual compounds are present as isolated octahedra.^{29,30} This structural change could be initiated by the introduction of water molecules into the crystal structure, where they form weak hydrogen bonds to the highly hygroscopic methylammonium cations leading to a bond dissociation between the crystal constituents. As a consequence, the unbound methylammonium iodide can readily escape the compound structure leaving behind a residual layer of lead iodide (Supporting Information 1). Indeed we observe that the X-ray diffraction pattern after thermal degradation resembles that of PbI₂.

It is conceivable that the hole-transporting layer (HTL), that forms the outermost layer in a typical perovskite solar cell, could have a protective effect on the perovskite structure by shielding it from atmospheric moisture, and by “sealing in” the volatile perovskite components preventing the thermally induced loss of the organic molecules. The extent of this protection will consequently depend on the hydrophobicity, permeability, and density of the hole-transporting material. These additional properties of the hole-transporter, which are largely unconnected to its electronic characteristics, may therefore have a strong impact on the overall solar cell stability.

We investigate three commonly employed hole-transporting materials (HTMs), spiro-OMeTAD, P3HT, and PTAA, and subject perovskite films coated with these hole-transporters to a temperature of 80 °C on a hot plate in ambient air. Solar cells will typically have to operate at temperatures up to 85 °C, so this test is within the normal operating range. Photographs of such films are shown in Figure 1. The first signs of degradation are visible after only 24 h (Figure 1a). After 96 h, the degradation has progressed significantly, where all perovskites

films coated with the organic hole-transporters have become predominantly yellow. The X-ray diffraction (XRD) patterns indicate that a loss of methylammonium iodide underlies the degradation and color change (Figure 1c and Supporting Information 2), because the diffraction patterns have transitioned from perovskite to PbI₂. For a film of undoped spiro-OMeTAD, this observed degradation is slower than for spiro-OMeTAD doped with Li-TFSI (Supporting Information 3). This suggests that the highly hygroscopic nature of the lithium-based dopant may have a significant role in introducing moisture into the perovskite structure, thus accelerating its degradation. We therefore stress the importance of developing nonhygroscopic hole-transporting materials for use in perovskite solar cells.

The breakdown of the perovskite structure is also clearly visible in the absorption spectra of devices with Li-spiro-OMeTAD as HTL (Figure 1b). Before heat exposure, the sample exhibits a strong absorption in the visible range from 750 to 450 nm characteristic of CH₃NH₃PbI_xCl_{3-x}. In the spectra taken after heat exposure, this absorption feature disappears. This correlates with a visible color change of the films (Figure 1a), which become almost transparent in the red region of the spectrum. The X-ray diffractograms taken before and after heat exposure (Figure 1c and Supporting Information 2) confirm that the discoloration of the perovskite films, which are characterized by their strongest diffraction peaks at 14.28° and 28.57°, correlates with a breakdown of the perovskite crystal structure. The residual film exhibits an XRD pattern and absorption spectrum similar to that of neat lead iodide, with its characteristic diffraction peak at 12.80° (Supporting Information 1).

Clearly, none of the typically employed HTMs are effective barriers against thermal degradation of methylammonium lead

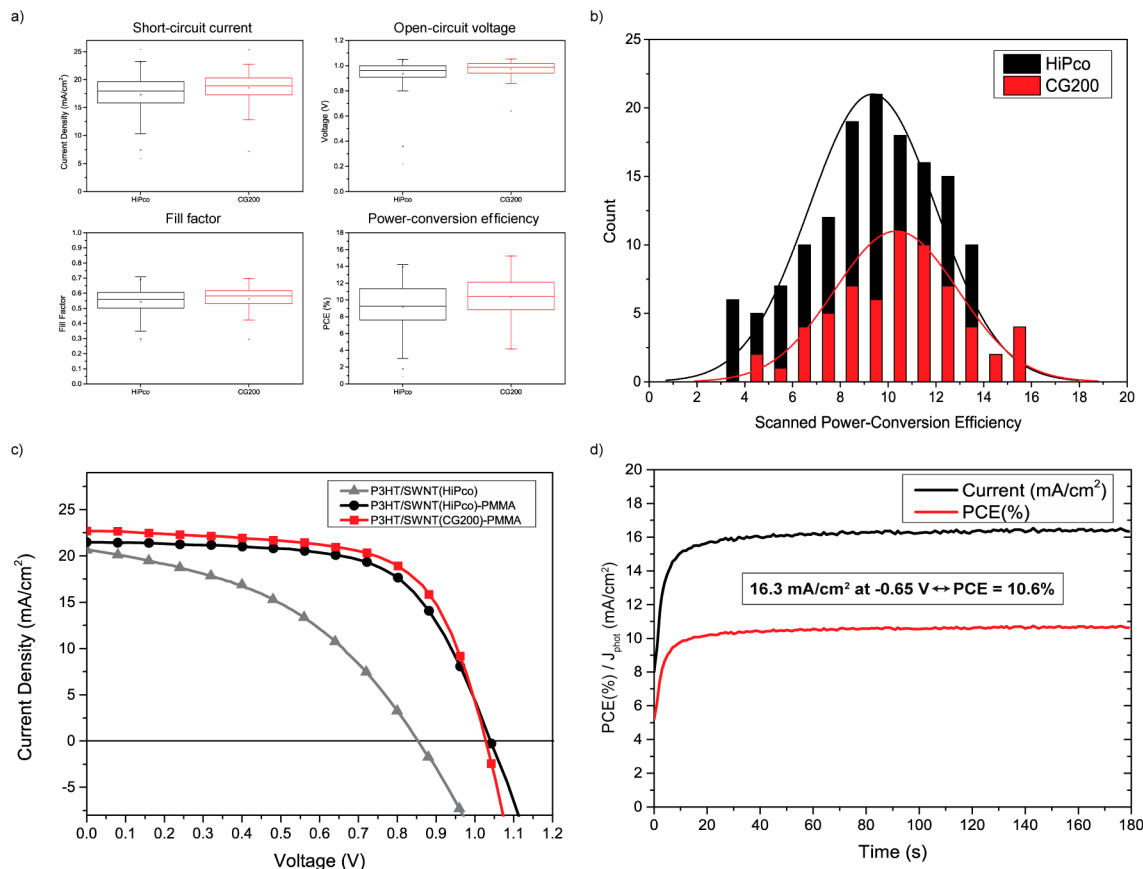


Figure 3. (a) Comparison of the performance parameters of devices with the two different nanotube types, HiPco and CG200. (b) Comparison of the performance distributions of the two different SWNT types combined with PMMA. (c) Plots of the current–voltage characteristics of the best-performing devices with a HTL composed of P3HT/SWNT(HiPco)-only (gray triangles); the stratified P3HT/SWNT(HiPco)-PMMA structure (black circles); and the P3HT/SWNT(CG200)-PMMA stratified HTL (red squares). The devices were scanned from forward bias to short-circuit at a rate of 0.24 V/s. (d) Stabilized-power output of a device with the optimized HTL based on CG200 SWNTs.

halide perovskite films in air. To counteract this degradation process we employ the insulating polymer poly(methyl methacrylate) (PMMA), which is hydrophobic and should therefore be capable of inhibiting the intrusion of moisture into the perovskite structure while simultaneously inhibiting the evaporation of the methylammonium iodide. We show in Figure 1 the effectiveness of PMMA as a protective layer, as compared to the standard HTMs; even after 96 h at 80 °C in air, we observe no significant difference in color, absorption, or crystal structure of the perovskite layer. Within the time frame of 96 h, PMMA can thus fully inhibit the degradation process.

Lacking π -conjugation, PMMA is not capable of transporting charge on its own and acts as an insulator. However, by combining PMMA with a highly conductive component, this insulator/hole-conductor composite may be able to retain the protective properties of PMMA while possessing selective charge collection properties similar to the organic hole-transporters. Single-walled carbon nanotubes (SWNTs) are an excellent candidate for the role of the charge transporting component due to their exceptional charge transport characteristics as well as their structural and chemical stability.³¹ Carbon nanotubes are generally insoluble, however when wrapped with a monolayer of P3HT, they form supramolecular nanohybrids (P3HT/SWNT) that are dispersible in common solvents and can be deposited by spin-coating.³² The functionalizing sheath of P3HT around the SWNTs also has an impact on their electronic properties and tends to make them predominantly p-

type in nature (Supporting Information 5),^{33,34} making them more likely to be a hole-selective p-type charge collection layer in a perovskite solar cell.

We sequentially coated perovskite films with P3HT/SWNTs and PMMA. In Figure 1, we demonstrate that the presence of functionalized SWNTs does not impact the protection effect of PMMA. The composite structure of P3HT/SWNTs and PMMA appears to protect the perovskite layer just as well as a neat film of PMMA resulting in no signs of degradation of the perovskite layer as deemed by the absorption and X-ray diffraction patterns.

We show the meso-superstructured solar cell (MSSC) structure^{3,9} studied here in Figure 2, where the hole collection layer is a P3HT/SWNT nanohybrid mesh, in-filled with PMMA, and capped with a silver electrode.

As a proof of principle for selective charge transport of photogenerated holes mediated by the functionalized SWNTs, we initially fabricated devices in which only an uncovered film of P3HT/SWNTs served as hole-transporting layer to the electrode, Figure 3 (P3HT/SWNT(HiPco)). Working devices dramatically outperform their control counterparts in which the metal cathode directly contacts the perovskite absorber (Supporting Information 4a). In the best-performing device, we observed remarkably high photocurrent of 20.8 mA/cm², indicating that efficient hole-transfer can occur through the nanohybrids, unhindered by their relatively low contact area with the perovskite. The best-performing device delivered a

scanned power-conversion efficiency of 7.4% and demonstrates that charge-selective transport is in fact supported by the polymer-functionalized SWNTs. Its performance is, however, limited by the low fill factor and low voltage, that most likely arise from recombination losses due to direct contact of the metal electrode to the perovskite, through the gaps between the P3HT/SWNT mesh. This also causes a very high failure rate of devices and thus leads to a poor average performance with a very broad distribution of $2.8 \pm 2.7\%$.

By depositing the PMMA matrix on top of the P3HT/SWNT layer, we fill the gaps within the nanohybrid network and prevent direct contact of the metal cathode with the perovskite absorber. The reduction of recombination losses and increase in shunt-resistance due to the presence of the PMMA layer leads to a significant increase in voltage and fill-factor. The average efficiency of 143 individual devices with this structure is $9.3 \pm 2.9\%$ with the best-performing device reaching a scanned power-conversion efficiency of 14.2% (Figure 3, Table 1).

Table 1. Performance Parameters of the Best-Performing Solar Cells with P3HT/SWNTs as Hole Transporter

HTL architecture	J_{sc} [mA/cm ²]	V_{oc} [V]	FF	max. PCE [%]	avg. PCE [%]
P3HT/SWNT (HiPco) only	20.65	0.85	0.42	7.4	2.8 ± 2.7
P3HT/SWNT(HiPco)-PMMA	21.49	1.04	0.63	14.2	9.3 ± 2.9
P3HT/SWNT(CG200)-PMMA	22.71	1.02	0.66	15.3	10.4 ± 2.6

In this device, the functionalized SWNTs were produced by the High Pressure Carbon monoxide (HiPco) process, yielding a ratio of 2:1 semiconducting to metallic nanotubes. We find that the presence of metallic species among the P3HT/SWNT nanohybrids does not seem to have introduced significant recombination losses, and because the hole conductivity of the HTL is one of the crucial factors for efficient charge collection, we tested further devices with a second type of metallic-enriched SWNTs (CoMoCAT, CG200). The more conductive SWNT species yields further improvement in the solar cell performance by systematically increasing the extracted photocurrent and open-circuit voltage (Figure 3). The average batch efficiency is $10.4 \pm 2.6\%$ with the champion device reaching a

scanned power-conversion efficiency of 15.3% (Figure 3, Table 1). The fairly broad device distribution is attributed to batch-to-batch variation of the perovskite absorber.

As has been recently observed, this kind of perovskite-based solar cell can exhibit hysteresis in the current–voltage curves with the measured current density depending on numerous factors such as the scanning direction, scanning speed, light-soaking, and preconditioning of devices at a forward bias.¹³ The cause for this behavior is yet to be determined, however, the time scales of the observed hysteresis suggest that this behavior might be related to migration of mobile ions in the perovskite material as reported by Unger et al.¹⁴ The scan speed affects therefore how strongly the scans in forward and reverse direction differ from each other. A reliable, scan-independent metric to determine the efficiency of such a device is the “stabilized power output” near the maximum power point.¹³ In Figure 3d, we also show the stabilized power output for a device with the optimized HTL based on CG200-SWNTs with a stabilized efficiency of 10.6%.

Using 96 h exposure to a temperature of 80 °C in air as a metric for how much the hole-transporting layer impacts upon the thermal stability, we tested the devices with the standard HTMs and the SWNT-PMMA composite for their photovoltaic performance before and after the thermal stressing, notably without any additional encapsulation. For devices with Li-TFSI doped spiro-OMeTAD (Li-spiro-OMeTAD), P3HT, and PTAA, the degradation of the perovskite progressed to the point that the devices did not generate any significant power output following the aging (we show the current–voltage curves before and after aging in the Supporting Information). In contrast, devices with the nanotube composite structure were still fully operational and achieve comparably high power conversion efficiencies before and after thermal stressing in air (Figure 4). This is in agreement with the corresponding absence of any discernible structural damage to the perovskite layer which we had observed earlier (Figure 1). Because the glass transition of PMMA is fairly low at 105 °C, it is likely that structural changes to the composite hole-extraction layer could occur under normal solar cell operating conditions. We therefore examined polycarbonate (PC) as an alternative protective matrix with a higher glass transition and melting point. Interestingly, the best-performing device with a polycarbonate matrix appeared to benefit from the heat exposure resulting in an increase in peak scanned performance

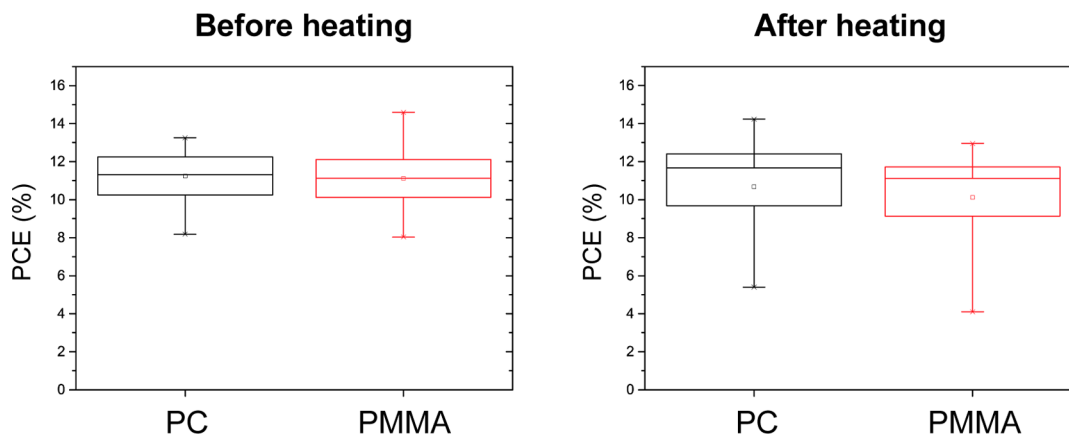


Figure 4. Temperature stressing of perovskite solar cells. Device performances before and after being exposed to 80 °C in air for 96 h, details are shown in Table 2.

from 13.3% to 14.3% after 96 h 80 °C stressing in air (Supporting Information 8). The average scanned PCE before and after thermal stressing changed from 11.2 to 10.7% and from 11.1 to 10.1% for PC and PMMA, respectively.

Table 2. Thermal Stressing

HTL architecture	max. PCE [%]	av. PCE [%]
PC before heating	13.3	11.2 ± 1.5
PMMA before heating	14.6	11.1 ± 2.3
PC after heating	14.3	10.7 ± 3.8
PMMA after heating	13.0	10.1 ± 3.2

Further evidence for a higher thermal stability of the SWNT-polymer structures is given by measuring the solar cell performance when operating at higher temperatures (Figure 5a). While the performance drops for both protective matrices,

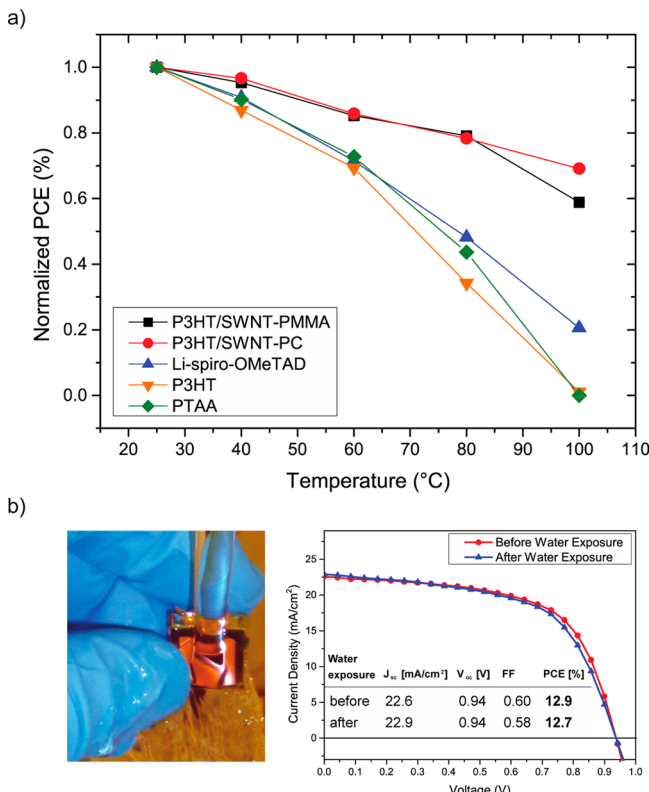


Figure 5. Temperature dependence and water resistance of perovskite solar cells. (a) Power conversion efficiency for perovskite solar cells employing the range of hole-extraction layers as a function of temperature. The power-conversion efficiency was measured after an equilibration time of 20 min at each temperature setting. (b) A photograph of a complete perovskite solar cell employing a PC-SWNT hole-extraction layer placed under a flowing tap with the active layer on the top side of the glass directly under the water flow (left-hand side). Current density–voltage plots measured under AM1.5 simulated sunlight of 100 mW cm^{-2} irradiance of the same perovskite solar cell before and after being placed under the running water for 60 s.

the decrease is significantly less than for the organic HTMs. Both protective matrices show strikingly similar performances at higher temperatures up to 80 °C, which indicates that the initial decline of about 20% from room temperature to 80 °C may occur independent of the material properties of the polymer matrices and could represent the temperature

coefficient for the perovskite cells, from this data being $\sim 0.33\text{%/}^{\circ}\text{C}$, similar to that of the thin film photovoltaics based on copper indium gallium (di)selenide (CIGS).³⁵ In the temperature range above 80 °C, a more significant drop in efficiency for the PMMA-based HTL is observed that is probably caused by approaching the glass transition temperature of the polymer ($T_g = 105 \text{ }^{\circ}\text{C}$). Structural damage to the protective matrix may hence be responsible for increased shunting due to direct contact between the electrode and the perovskite (Supporting Information 9a).

Similar to the 96 h exposure to heat, we observe that the devices with the PC matrix experience a slight increase in performance after having cooled down to room temperature. In contrast, though still operational, the devices with a PMMA matrix suffer a significant decrease in efficiency after being heated to 100 °C, as we show in Supporting Information (Figure S9b). The damage to the devices with Li-TFSI doped spiro-OMeTAD, P3HT, and PTAA appeared to be irreversible as we observed no recovery of these devices after cooling.

As previously mentioned, moisture stability is another critical concern for this class of perovskite materials because methylammonium iodide is water-soluble and its interaction with moisture can initiate the breakdown of the perovskite crystal structure. Here, we may also expect the “water-resistant” PMMA or PC to offer enhanced protection of the solar cell. As an initial test, we exposed working unsealed devices to a steady stream of running water (Figure 5b) and tested the photovoltaic performance before and after exposure. While devices coated with Li-TFSI doped spiro-OMeTAD quickly discolor (Supporting Information 10), the devices employing PC-SWNT charge extraction layers show no sign of damage upon water exposure, and the devices operated with close to identical performance before and after exposure (Figure 5c).

In summary, we have addressed the issues of thermal and moisture stability of perovskite solar cells by employing a new family of p-type charge transport materials for perovskite solar cells, functionalized SWNTs embedded in an inert polymer matrix. The structure achieves competitive power-conversion efficiencies and crucially, offers unprecedented resilience against thermal stressing and moisture ingress. Coupled with appropriate external encapsulation strategies, this nanotube–polymer composite could be a major step forward in the drive toward achieving 25 years operation lifetime for perovskite solar cells. Beyond perovskite solar cells, the composite of functionalized SWNTs within an inert polymer matrix could prove to be an interesting avenue for printable contacts for other photovoltaic technologies and light-emitting devices. This work should now also encourage renewed effort in employing functionalized SWNTs in conjunction with highly resilient polymer matrices.

Methods. *SWNT Functionalization.* Powdered single-walled carbon nanotubes (SWNTs) produced by the HiPco process were purchased from Carbon Nanotechnologies Incorporated (CNI; now Unidym) with lengths of 100–1000 nm and an intermediate diameter distribution of 0.8–1.2 nm. The samples used in this work were purchased as “purified” tubes (<15 wt % iron catalyst impurities). The second type of SWNTs, SWeNT CG200, was purchased from Sigma Aldrich, has a diameter range from 0.7–1.4 nm and a relative purity of 90% as the percentage of carbon that is present as SWNTs. 3.0 mg of rr-P3HT (Rieke Metals Inc., weight-average molecular weight, $M_w = 50\,000 \text{ g mol}^{-1}$ and regioregularity = 95%) was dissolved in 5.00 mL of chlorobenzene and sonicated in a bath

sonicator for 60 min. 2.5 mg of SWNTs was added, as purchased, to the dissolved polymer solution and treated with an ultrasonic probe for 10 min. The mixture was subsequently centrifuged for 8 min at 10 000g to remove nonfunctionalized SWNTs and other carbonaceous particles. The precipitate was discarded while the supernatant was recovered. In order to remove the excess polymer according to the solvent extraction technique detailed by Schuettforth et al.,³² 15 mL of toluene was added. The mixture was then mildly heated for 60 min to induce aggregation of the functionalized SWNTs. The aggregates were then removed by centrifugation (4 min at 16 000 g). This time the supernatant containing excess polymer was discarded and the precipitate was recovered and redispersed in 5 mL of toluene. This mixture was then sonicated for 15 min in the ultrasonic bath to fully redissolve nonwrapped polymers. After the sonication, the mixture was mildly heated for 15 min to induce aggregation and then centrifuged for 4 min at 16 000g. The supernatant was then discarded. This procedure from bath sonication to centrifugation was repeated three times to remove all excess polymer resulting in the final supernatant being fully transparent. The final pellet consists of 2.0–2.2 mg of functionalized nanotubes, which are dispersed in 16 mL of chloroform. Immediately prior to spin-coating, the chloroform dispersion was sonicated with an ultrasonic probe for 2 min at low intensity (~10% of amplitude) to break up clusters and bundles.

Solar Cell Fabrication. A glass wafer with a layer of fluorine-doped tin oxide (FTO) was first cleaned with detergent and deionized water, then with acetone and isopropanol. Thereafter it was treated for 10 min in O₂ plasma. The electron-accepting TiO₂ compact layer was spin-coated (2000 rpm for 60 s) from a mildly acidic (after addition of 12 μM HCl) solution of titanium isopropoxide in anhydrous ethanol and sintered at 500 °C. The low-temperature meso-structured scaffold was afterward deposited by spin-coating (2500 rpm for 60 s) from a colloidal dispersion of 20 nm Al₂O₃ nanoparticles in isopropanol followed by drying at 150 °C.⁹ After having cooled down to room temperature, the perovskite layer was spin-coated and dried at 100 °C for 45 min. Following this step, the hole transport layer was deposited by spin-coating. For the two-layer structure of SWNT and polymer, first the SWNT layer was deposited dynamically by drop-by-drop spin-coating (3000 rpm for 90 s) of 200 μL. Followed immediately by the deposition of the poly(methyl methacrylate) (PMMA, 50 mg/mL in toluene) layer or the poly(bisphenol A carbonate) (PC, 60 mg/mL in chlorobenzene) layer by spin-coating (2000 rpm for 60 s). The other hole transporter were also deposited by spin-coating: 8 wt % spiro-OMeTAD in chlorobenzene with added 6.8 μL/ml *tert*-butylpyridine (*t*Bp) and 20.4 μL/ml lithium bis(trifluoromethanesulfonyl)imide (Li-TFSI) from a solution of 170 mg/mL in acetonitrile; 15 mg/mL P3HT in dichlorobenzene with added 3.4 μL/ml *t*Bp and 6.8 μL/ml Li-TFSI from 28.3 mg/mL Li-TFSI/acetonitrile; 15 mg/mL PTAA ($M_w = 23.3k$) in toluene with added 6.8 μL/ml and 13.6 μL/ml Li-TFSI from 28.3 mg/mL Li-TFSI/acetonitrile. Spiro-OMeTAD was spin-coated at 2000 rpm for 60 s, and P3HT and PTAA were spin-coated at 3000 rpm for 30 s. Finally, gold or silver electrodes were thermally evaporated onto the HTL.

Current–Voltage Measurements. For measuring the performance of the solar cells, simulated AM 1.5 sunlight was generated with a class AAB ABET solar simulator calibrated to give simulated AM 1.5 of 100.0 mW cm^{−2} equivalent irradiance, using an NREL-calibrated KG5 filtered silicon reference cell.

The mismatch factor was calculated to be 1.02 between 300 to 900 nm, which is greater than the operating range of both the KG5 filtered silicon reference cell and the perovskite test cells.⁹ The current–voltage curves were recorded with a sourcemeter (Keithley 2400, U.S.A.). The solar cells were masked with a metal aperture defining the active area (0.063 cm²) of the solar cells. Additionally, by removing active material between individual cells on the same glass substrate, single-cell contributions were ensured. Measurements were done in a light-tight sample holder to minimize any edge effects and ensure that the reference cell and test cell are located during measurement in the same spot under the solar simulator.

■ ASSOCIATED CONTENT

§ Supporting Information

More detailed information regarding the degradation of bare methylammonium lead iodide/chloride, the degradation of devices with P3HT and PTAA, of undoped spiro-OMeTAD; device performance of PMMA-only control devices, energy scheme, SWNT-film deposition, reproducibility and variability of device performance, JV-characteristics of best-performing devices of all investigated HTLs, thermal stability current–voltage characteristics, thermal dependence of device performance and water stability. This material is available free of charge via the Internet at <http://pubs.acs.org>.

■ AUTHOR INFORMATION

Corresponding Author

*E-mail: h.snaith1@physics.ox.ac.uk.

Author Contributions

All authors contributed to the writing of the manuscript. S.N.H. conceived and carried out the experiments with help from T.L., G.E.E., and S.D.S.; H.J.S. and R.J.N. conceived and supervised the project. All authors discussed the results and commented on the manuscript.

Notes

S.N.H., R.J.N., and H.J.S. are named inventors on British Patent Application No. 1404840.9, (filed 18 March 2014), which is related to the techniques described in this article. The authors declare no competing financial interest.

■ ACKNOWLEDGMENTS

This work was partially funded by the European Community's Seventh Framework Programme (FP7/2007–2013) under Grant Agreement 246124 of the SANS project and by the Engineering and Physical Sciences Research Council. The authors want to thank James M. Ball for taking the photographs and Nakita K. Noel for the helpful discussions.

■ REFERENCES

- (1) Chu, S.; Majumdar, A. *Nature* **2012**, *488*, 294–303.
- (2) Weickert, J.; Dunbar, R. B.; Hesse, H. C.; Wiedemann, W.; Schmidt-Mende, L. *Adv. Mater.* **2011**, *23*, 1810–1828.
- (3) Lee, M. M.; Teuscher, J.; Miyasaka, T.; Murakami, T. N.; Snaith, H. J. *Science* **2012**, *338*, 643–647.
- (4) Kim, H.-S.; Lee, C.-R.; Im, J.-H.; Lee, K.-B.; Moehl, T.; Marchioro, A.; Moon, S.-J.; Humphry-Baker, R.; Yum, J.-H.; Moser, J. E.; Grätzel, M.; Park, N.-G. *Sci. Rep.* **2012**, *2*, 591.
- (5) Im, J.-H.; Lee, C.-R.; Lee, J.-W.; Park, S.-W.; Park, N.-G. *Nanoscale* **2011**, *3*, 4088–4093.
- (6) Liu, M.; Johnston, M. B.; Snaith, H. J. *Nature* **2013**, *501*, 395–398.

- (7) Eperon, G. E.; Burlakov, V. M.; Docampo, P.; Goriely, A.; Snaith, H. J. *Adv. Funct. Mater.* **2014**, *24*, 151–157.
- (8) Burschka, J.; Pellet, N.; Moon, S.-J.; Humphry-Baker, R.; Gao, P.; Nazeeruddin, M. K.; Grätzel, M. *Nature* **2013**, *499*, 316–319.
- (9) Ball, J. M.; Lee, M. M.; Hey, A.; Snaith, H. J. *Energy Environ. Sci.* **2013**, *6*, 1739.
- (10) Stranks, S. D.; Eperon, G. E.; Grancini, G.; Menelaou, C.; Alcocer, M. J. P.; Leijtens, T.; Herz, L. M.; Petrozza, A.; Snaith, H. J. *Science* **2013**, *342*, 341–344.
- (11) Wang, J. T.-W.; Ball, J. M.; Barea, E. M.; Abate, A.; Alexander-Webber, J. a; Huang, J.; Saliba, M.; Mora-Sero, I.; Bisquert, J.; Snaith, H. J.; Nicholas, R. J. *Nano Lett.* **2014**, *14*, 724–730.
- (12) Wojciechowski, K.; Saliba, M.; Leijtens, T.; Abate, A.; Snaith, H. J. *Energy Environ. Sci.* **2014**, *7*, 1142–1147.
- (13) Zhou, H.; Chen, Q.; Li, G.; Luo, S.; Song, T. -b.; Duan, H.-S.; Hong, Z.; You, J.; Liu, Y.; Yang, Y. *Science* **2014**, *345*, 542–546.
- (14) Snaith, H. J.; Abate, A.; Ball, J. M.; Eperon, G. E.; Leijtens, T.; Noel, N. K.; Stranks, S. D.; Wang, J. T.-W.; Wojciechowski, K.; Zhang, W. *J. Phys. Chem. Lett.* **2014**, *5*, 1511–1515.
- (15) Unger, E. L.; Hoke, E. T.; Bailie, C. D.; Nguyen, W. H.; Bowring, A. R.; Heumuller, T.; Christoforo, M. G.; McGehee, M. D. *Energy Environ. Sci.* **2014**, DOI: 10.1039/C4EE02465F.
- (16) Juárez-Pérez, E. J.; Wussler, M.; Fabregat-Santiago, F.; Lakus-Wollny, K.; Mankel, E.; Mayer, T.; Jaegermann, W.; Mora-Sero, I. *J. Phys. Chem. Lett.* **2014**, *5*, 680–685.
- (17) Heo, J. H.; Im, S. H.; Noh, J. H.; Mandal, T. N.; Lim, C.-S.; Chang, J. A.; Lee, Y. H.; Kim, H.; Sarkar, A.; Nazeeruddin, M. K.; Grätzel, M.; Seok, S. Il. *Nat. Photonics* **2013**, *7*, 486–491.
- (18) Bi, D.; Yang, L.; Boschloo, G.; Hagfeldt, A.; Johansson, E. M. J. *J. Phys. Chem. Lett.* **2013**, *4*, 1532–1536.
- (19) Liu, D.; Kelly, T. L. *Nat. Photonics* **2013**, *8*, 133–138.
- (20) Dualeh, A.; Moehl, T.; Nazeeruddin, M. K.; Grätzel, M. *ACS Nano* **2013**, *7*, 2292–2301.
- (21) Abate, A.; Hollman, D. J.; Teuscher, J.; Pathak, S.; Avolio, R.; D'Errico, G.; Vitiello, G.; Fantacci, S.; Snaith, H. J. *J. Am. Chem. Soc.* **2013**, *135*, 13538–13548.
- (22) Burschka, J.; Dualeh, A.; Kessler, F.; Baranoff, E.; Cevey-Ha, N.-L.; Yi, C.; Nazeeruddin, M. K.; Grätzel, M. *J. Am. Chem. Soc.* **2011**, *133*, 18042–18045.
- (23) Leijtens, T.; Lim, J.; Teuscher, J.; Park, T.; Snaith, H. J. *Adv. Mater.* **2013**, *25*, 3227–3233.
- (24) Abate, A.; Leijtens, T.; Pathak, S.; Teuscher, J.; Avolio, R.; Errico, M. E.; Kirkpatrick, J.; Ball, J. M.; Docampo, P.; McPherson, I.; Snaith, H. J. *Phys. Chem. Chem. Phys.* **2013**, *15*, 2572–2579.
- (25) Di Giacomo, F.; Razza, S.; Matteocci, F.; D'Epifanio, A.; Licoccia, S.; Brown, T. M.; Di Carlo, A. *J. Power Sources* **2014**, *251*, 152–156.
- (26) Christians, J. a; Fung, R. C. M.; Kamat, P. V. *J. Am. Chem. Soc.* **2014**, *136*, 758–764.
- (27) Noh, J. H.; Im, S. H.; Heo, J. H.; Mandal, T. N.; Seok, S. Il. *Nano Lett.* **2013**, *13*, 1764–1769.
- (28) Leijtens, T.; Eperon, G. E.; Pathak, S.; Abate, A.; Lee, M. M.; Snaith, H. J. *Nat. Commun.* **2013**, *4*, 2885.
- (29) Mitzi, D. B. In *Progress in Inorganic Chemistry*; John Wiley & Sons, Inc.: New York, 2007; pp 1–121.
- (30) Vincent, B. R.; Robertson, K. N.; Cameron, T. S.; Knop, O. *Can. J. Chem.* **1986**, *1042–1046*.
- (31) Dürkop, T.; Getty, S. A.; Cobas, E.; Fuhrer, M. S. *Nano Lett.* **2004**, *4*, 35–39.
- (32) Schuettfert, T.; Snaith, H. J.; Nish, A.; Nicholas, R. J. *Nanotechnology* **2010**, *21*, 25201.
- (33) Dissanayake, N. M.; Zhong, Z. *Nano Lett.* **2011**, *11*, 286–290.
- (34) Dabera, G. D. M. R.; Jayawardena, K. D. G. I.; Prabhath, M. R. R.; Yahya, I.; Tan, Y. Y.; Nismy, N. A.; Shiozawa, H.; Sauer, M.; Ruiz-Soria, G.; Ayala, P.; Stolojan, V.; Adikaari, a a D. T.; Jarowski, P. D.; Pichler, T.; Silva, S. R. P. *ACS Nano* **2013**, *7*, 556–565.
- (35) Virtuani, A.; Pavanello, D.; Friesen, G. *Eur. Photovoltaic Sol. Energy Conf., Proc. Int. Conf. 25th* **2010**, *4248–4252*.